Rapporti Tecnici INAF
INAF Technical Reports

Number	174
Publication Year	2022
Acceptance in OA@INAF	2022-07-18T11:15:34Z
Title	Hyperhemispheric Lens Geometric Calibration
Authors	CORAN, GIACOMO; SIMIONI, EMANUELE; PERNECHELE, Claudio; LESSIO, Luigi
Affiliation of first author	O.A. Padova
Handle	http://hdl.handle.net/20.500.12386/32518; https://doi.org/10.20371/INAF/TechRep/174

TR01 – HYPEREMISPHERIC LENS GEOMETRIC CALIBRATION

29/06/2022
G. Coran[1], E. Simioni[1], C. Pernechele[1], L. Lessio[1]

(1) INAF OSSERVATORIO ASTRONOMICO DI PADOVA

Index of contents

1 INTRODUCTION

1.1 Approval

Edited by	G. Coran
Revised by	E. Simioni
Approved by	C. Pernechele

1.2 Acknowledgments

1.3 Reference Documents

RD 1   CREMONESE, G., CAPACCIONI, F., CAPRIA, M., & AL. (2020). SIMBIO-SYS: SCIENTIFIC CAMERAS AND SPECTROMETER FOR THE BEPICOLOMBO MISSION. *SPACE SCIENCE REVIEWS, 216*(5), 1-78. DOI:10.1007/S11214-020-00704-8

RD 2   PERNCHELE, C. (2016). HYPER HEMISPHERIC LENS. *OPTICS EXPRESS, 24*(5), 5014-5019. DOI:10.1364/OE.24.005014

RD 3   PERNECHELE, C. (2018). *INTRODUCTION TO PANORAMIC LENSES* (VOL. SL38). (S. O.-O. ENGINEERS, A CURA DI) BELLINGHAM, WASHINGTON, USA: SPIE PRESS. DOI:10.1117/3.2322575

RD 4   RUFLI, M., & AL. (2008). AUTOMATIC DETECTION OF CHECKERBOARDS ON BLURRED AND DISTORTED IMAGES. *2008 IEEE/RSJ INTERNATIONAL CONFERENCE ON INTELLIGENT ROBOTS AND SYSTEMS, IROS*, (P. 3121-3126). NICE, FRANCE. DOI:10.1109/IROS.2008.4650703

RD 5   SCARAMUZZA, D. (S.D.). *OCAMCALIB*. TRATTO DA OMNIDIRECTIONAL CAMERA CALIBRATION TOOLBOX FOR MATLAB: HTTPS://SITES.GOOGLE.COM/SITE/SCARABOTIX/OCAMCALIB-OMNIDIRECTIONAL-CAMERA-CALIBRATION-TOOLBOX-FOR-MATLAB

RD 6   SCARAMUZZA, D., MARTINELLI, A., & SIEGWART, R. (2006). A TOOLBOX FOR EASILY CALIBRATING OMNIDIRECTIONAL CAMERAS. *IEEE/RSJ INTERNATIONAL CONFERENCE ON INTELLIGENT ROBOTS AND SYSTEMS*, (P. 5695-5701).

RD 7   SIMIONI, E., & AL. (2019). SIMBIO-SYS/STC STEREO CAMERA CALIBRATION: GEOMETRICAL DISTORTION. *REVIEW OF SCIENTIFIC INSTRUMENTS, 90*(4). DOI:10.1063/1.5085710

1.4 Acronyms

BPL	Bifocal Panoramic Lens.
FOV	Field Of View
IFOV	Instantaneous Field Of View
LM	Levenberg-Marquadt
OCAMCALIB	Omnidirectional Toolbox
SSRE	Sum of Squared Reprojection Errors
SVD	Singular Value Decomposition

2 SCOPE OF THE TR

In this report we will show the calibration procedure and the obtained results for the definition of the intrinsic parameters of a wide-angle lens through the use of a set of acquisitions of a well-known calibration target. In this case the method is applied to INAF payload panoramic hereafter called BPL (Bifocal Panoramic Lens) **[RD 2]**.

3 CALIBRATION METHOD

Since we are working on a camera, the BPL, which represents a non-central projection (i.e. it does not have a single effective viewpoint or projection center) we cannot apply a common pinhole or 360 prospective model.

On the other side it is possible to model it as orthogonal projection followed by a reflection through a symmetric mirror defined by polynomial coefficients. This approach is developed in MATLAB Omnidirectional Toolbox (OCAMCALIB) **[RD 6]**.

The approach is based on the acquisitions of images of a well-known target uniformly distributed in the FOV (Field Of View) of the camera.

Thanks to this approach we were able, without the use of rotational or mechanical components (i.e. hexapod **[RD 1]** or series of rotational system to menage mirrors and light source [**RD 7**]to obtain the intrinsic parameters (the model of the camera) and the target parameters (the position and the orientation of the target in the world space), and, with a further improvement, even data on the relation between various parameters and the calibration errors. From those data with a later iterative analysis we were able to measure the values for the constants defining the mapping function of the BPL.

The camera model, with an introduction on the single effective viewpoint, as well as the particular case of the BPL will be discussed in the next section 3.1, while the intrinsic and target calibration will be shown in section 3.2. In 3.3 we will briefly discuss the requirement of the mapping function.

3.1 Geometrical projective model

3.1.1 Single effective viewpoint constrains

As described in the previous section BPL does not have the central characteristics; this means that it is not possible to model it as a single point projective system associated to a mirror. Central and not central design are showed in Figure 3.1. For a catadioptric camera to be a central system, the following arrangements must be satisfied: for a hyperbolic mirror, the camera optical center has to coincide with the focus of the hyperbola; for a parabolic mirror camera, the lens should be orthographic. Cameras using fisheye lenses are not in general central systems, but they very well approximate the single viewpoint property. In the case of the BPL the non-central configuration implies the necessity to find the relation between a given 2D pixel point of the image plane and the 3D direction coming from the equivalent mirror surface effective viewpoint. This can be performed by OCAMCALIB [**RD 5**] under limited assumption.
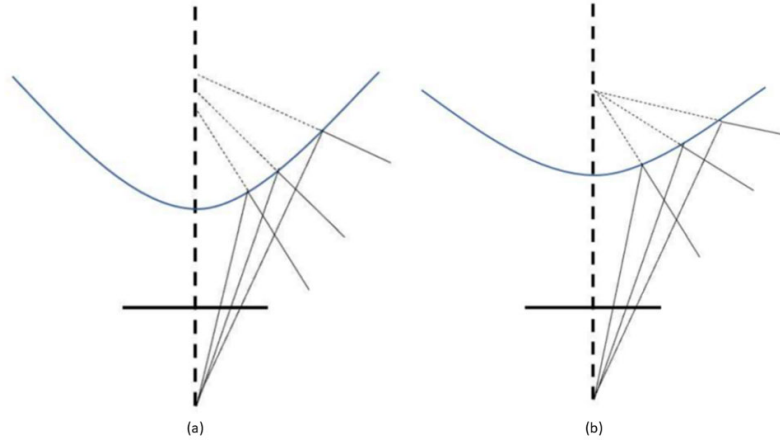
FIGURE 3.1 *IN (A) A CAMERA-MIRROR ASSEMBLY NON-CENTRAL (I.E. NON-SINGLE EFFECTIVE VIEWPOINT) SYSTEM WHERE THE OPTICAL RAYS COMING FROM THE CAMERA AND REFLECTED BY THE MIRROR SURFACE DO NOT INTERSECT INTO A UNIQUE POINT; IN (B) A CENTRAL CAMERA WHERE THE SINGLE EFFECTIVE VIEWPOINT PROPERTY IS PERFECTLY VERIFIED; IN BOTH CASES A NON-ORTHOGRAPHIC PROJECTION IS USED TO MODEL THE IMAGE PLANE FORMATION*

3.1.2   Camera model

The model proposed associates the homogenous coordinates $u' \in \mathrm{R}^3$ in the sensor reference system (centered in C' in Figure 3.2) to a coaxial reference system (C'', called here after "center of the camera") following an affine transformation:

$$u'' = Au' \qquad (3.1)$$

where $A \in \mathrm{R}^{3x3}$ is an affine transformation which well approximates possible off-axis misalignment between the orthonormal projection and the equivalent mirror symmetrical axis.

The relation between a 3D point $X \in \mathrm{R}^4$ (expressed in homogeneous coordinates) and the coaxial reference system coordinates can be expressed by:

$$v = g(u'') \qquad (3.2)$$

where the versor v represents the optical ray associated to the pixel and g is rotationally symmetric non-linear function representing the mirror. In the case of non-central cameras (see Figure 3.2b) this definition is not associated to a central point. In the case of central cameras (see Figure 3.2c) the versor satisfied even the equation:

$$\lambda v = PX, \lambda > 0 \qquad (3.3)$$

where, $P \in \mathrm{R}^{3x4}$ is the projection matrix centered for catadioptric systems in the focus of the parabolic or hyperbolic shape mirror.
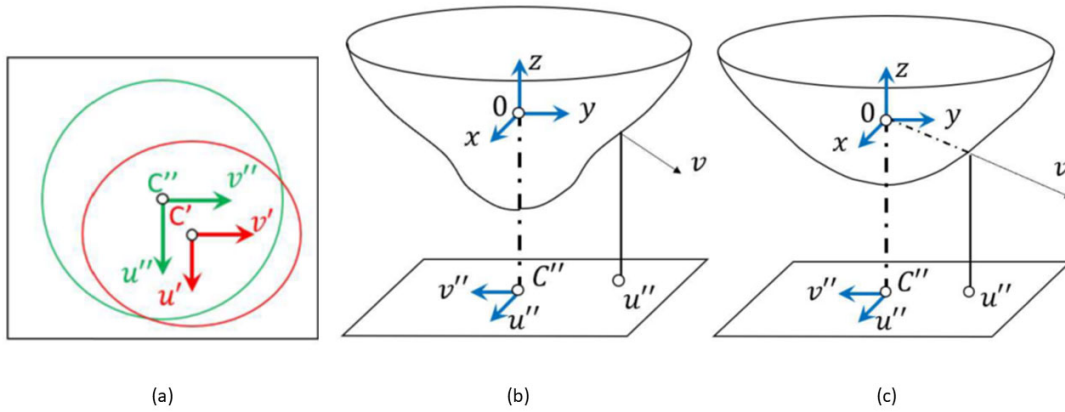
FIGURE 3.2 *IN (A) THE SENSOR PLANE IN METRIC COORDINATES (IN GREEN) AND THE OVERLAPPED CAMERA IMAGE PLANE (IN RED). THE TWO SYSTEMS ARE RELATED BY AN AFFINE TRANSFORMATION. IN (B) GENERIC NON-CENTRAL CAMERA MODEL BASED ON RADIAL SYMMETRICAL MIRROR. IN (C) CENTRAL MODEL CONVERGENT ON THE ORIGIN REFERENCE SYSTEM*

In the case of the omnidirectional camera it is assumed that the function g is rotationally symmetric with respect to the sensor normal axis. Following this Eq (3.2) assumption can be rewritten as:

$$\theta = \phi(\rho) \tag{3.4}$$

where ρ is the distance in pixels of the projected point from the camera center in the u'', v'' reference system and θ is the zenith angle of the chief ray respect to the horizon plane, positive in the hemisphere full covered.
We propose two different solutions and the definition of the ϕ function. Both the solutions use an N order polynomial here after indicated as:

$$\mathbf{p}(\rho) = \sum_{i=0}^{N} p_i \rho^i \tag{3.5}$$

or as FPF (Forward Projective Function).
First solution is a simple "direct model" where the chief ray is defined by the same polynomial function:

$$\theta = p(\rho) \tag{3.6}$$

A more "physical approach" defines the chief ray as:

$$\tan(\theta) = -\frac{\rho}{p(\rho)} \tag{3.7}$$

The direct model returns a more constrained camera model. The simplicity of the model allows for instance to add as vinculum the monotony of the IFoV (simple derivative of the p function). On the other side, physical approach reaches the best performance but making not possible to impose any additive vinculum. This brings to a not correct interpretation of the geometry of the camera model in the outer regions of the field of view. The two models' main equations, including the solver used in the nonlinear regression methods of the different stages of the calibration are reported in Table 1.

Direct Model	
Chief Ray	$\theta = p(\rho)$
IFoV	$\dot{\theta} = \dot{p}(\rho)$
Solver	$p_0 - \theta + p_1\rho + \cdots + p_N\rho^N = 0$
Physical Model	
Chief Ray	$\tan(\theta) = \dfrac{\rho}{p(\rho)}$
IFoV	$\dot{\theta} = -\dfrac{p + \dot{p}\rho}{p^2 + \rho^2}$
Solver	$p_0 + (p_1 - \tan(\theta))\rho + \cdots + p_N\rho^N = 0$

TABLE 1 *MAIN EQUATIONS OF THE SIMPLE AND PHYSICAL MODELS DEVELOPED*

Table 1 reports even the IFoV as derivative of the zenith angle with respect to the pixel distance from the center. Note that while in the first case it assumes a polynomial form for the chief ray, in the physical model it is defined by a rational model which reaches at denominator two time the magnitude of the polynomial order.

3.2 OCAMCALIB estimation method

We used an estimation method developed by Scaramuzza on Matlab.
The method utilizes a code able to recognize a chessboard inside an image acquired with a generic lens (in this approach a hyperhemispheric one) and detect the corner points thanks to a Harry extractor.

3.2.1 Automatic or Manual Extraction

First, we must load the images and extract the corner points, which are the crossing point within four squares. It is required to define the number of squares along the two axes of the chessboard and the dimension of the side of a square, which in our case is 42mm.
The code can automatically identify the corners, asking for user supervision only if it is not able to recognize all the corners that should be present. Corners are detected following a specific approach based on Harris detection The algorithm works by analyzing the eigenvalues of the 2D discrete structure tensor matrix at each image pixel and flagging a pixel as a corner when the eigenvalues of its structure tensor are sufficiently large. The algorithm has a satisfying detection rate of 95% and an accuracy less than 0.5 px [**RD 4**].
 However, the user is always able to identify manually all the corners.
The code requires an initial central point for the lens, with a default option being the central point of the image, so half the height and half the width.

3.2.2 Calibration

The code calibrates the optical system starting from the images.
It estimates at the same time the intrinsic parameters and the angular target parameters (position and orientation of the chessboards in the real world) by minimizing the residuals of the projected points via Singular Value Decomposition (SVD) taking advantage of to the orthogonality of the grid. In

this way the code defines completely the rototranslation from the reference system of the target to the camera reference system.

As intrinsic parameters it considers the affine transformation and the radial function, described in Eq.(3.6), parametrized with a polynomial model which DOFs (degree of freedom) can be chosen by the user. For the following analysis, a fourth-degree polynomial equation was used. The final missing parameters of the positions of the chessboards in the camera space are then defined estimating the polynomial parameters via a simple least-squares solution, which also better defines the polynomial solution and the affine transformation.

The code returns this first estimation of the coefficients.

3.2.2.1   Find Center

The model is strongly dependent on the center position of the image on the sensor (Figure 3.2 (a)) which, when incorrectly defined, not only corresponds to misalignment of the symmetric axis but also has the effect of increasing the weight of the reprojection error.

Via iterative image analysis the code is able to identify the true coordinates of the average center of the lens on the sensor minimizing globally the Sum of Squared Reprojection Errors (SSRE), making up for the chance of a lens not centered with the sensor. This step is the bottleneck in the code speed: tests showed an average duration of 24 hours for a set of 45 images.

3.2.2.2   Calibration Refinement

Once the image center is obtained, we can recalibrate the polynomial equation with the newly acquired information. The affine transformation, the polynomial definition of the mirror and the position and attitude of the targets are defined by non-linear optimization of the residuals thanks to Levenberg-Marquadt (LM) approach. From the estimated solution the algorithm refines the target and intrinsic parameters separately in a two steps iterative process, firstly refining the target parameters ignoring the intrinsic ones and the using the just estimated target parameters to refine the intrinsic ones. The results obtained with this step usually greatly improve the estimation obtained with the first calibration.

3.2.3   Reprojection on Images and Extrinsic Validation

The code is able the to re-project the corners re-calculated with the new polynomial calibration on the images, reconstructing the chessboards as in Figure 3.3 and showing the deviation from the initially detected corners, visible in Figure 3.4.
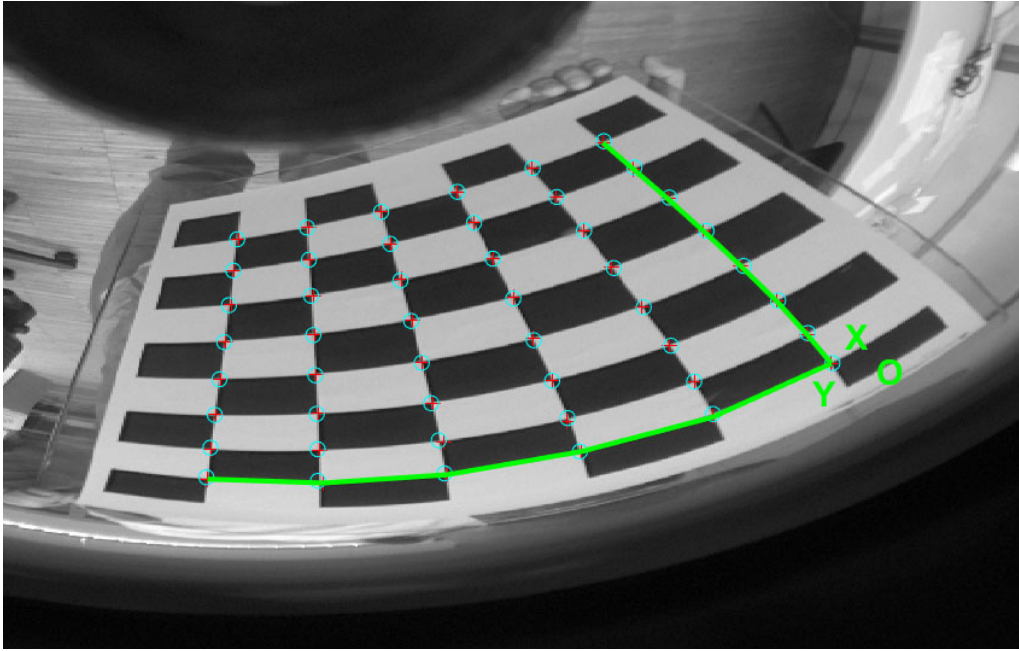
FIGURE 3.3: *EXAMPLE OF RECONSTRUCTED CHESSBOARD WITH THE INITIALLY DETECTED CORNERS IN RED AND RECOMPUTED CORNERS IN CYAN*
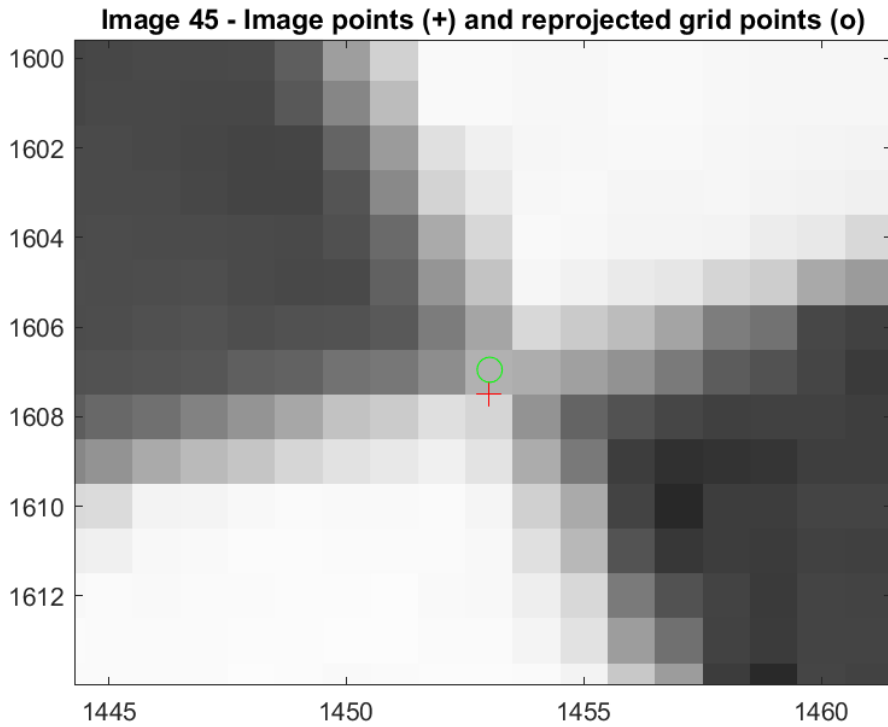

FIGURE 3.4 *EXAMPLE OF DEVIATION BETWEEN THE INITIAL AND THE RECOMPUTED CORNERS*

3.2.4 Intrinsic Parameters Visualization

The code can display the 3-D positions of the chessboards with respect to lens, as well as the recalibration errors, the forward projection function, and the angle of the optical ray with respect to distance from the image center in pixels.

The original code was modified in order to display additional plots.
The relation between the zenith angle and the recalibration errors is important, showing if the method is working to determine the position of the corners with precision even at high zenith angles where the anamorphism of the lens is higher. The plot showing the relation between the azimuthal angle and the recalibration errors can display the eventuality of a lens out of focus towards a specific direction. The IFoV was calculated from the polynomial equation and can be displayed with our addendum. It is also possible to print all the detected corners from all the images on a single image with a color gradient showing the magnitude of the recalibration errors.

3.3 Common mapping function

As described in *"Introduction to Panoramic Lenses"* [**RD 3**], the "perfect" undistorted map of the object space is given by:

$$\rho(Z) = d\tan(Z). \qquad (3.8)$$

Every point in the space is mapped so that they maintain the same angular distribution into the focal plane and object straight lines remain straight (distortion free) in the image. This function is known as "perspective projection" and it is not meaningful for wide zenith angles because the focal plane would be infinitely wide, and the entrance pupil would be completely obscured at $Z = 90°$.
Then, to make a wide-angle lens useful for some applications, some degree of image distortion must be accepted, and this is done by adjusting the mirror curvature and asphericity.

The most general lens mapping function has the following form:

$$\rho(Z) = dk_1\,sin(k_2 Z) \qquad (3.9)$$

where k_1 and k_2 are dimensional coefficients. Within this class of mapping functions, high compression of the marginal objects is present. We cite two types of projection which belong to this type of mapping functions:
• **equisolid angle projection** (k1=2, k2=0.5), i.e. R=2 f(0) sin(θ/2), which maintains surface relations. Each pixel in the detector subtends an equal solid angle, i. e. an equal area on the unit sphere.
• **orthographic projection** (k1=k2=1) where R= f(0) sin(θ). This mapping function maintains planar illuminance. In this projection the marginal fields are extremely compressed at the focal plane and make sense only for θ < 90°.

4 APPLICATION ON THE HEMISPHERIC LENS

4.1 Lens description

To test the method, we analyzed images gathered with a particular panoramic lens, called Bifocal Panoramic Lens (BPL), designed by our Institute [**RD 2**], displayed in Figure 4.1. This lens is a peculiar version of a double-reflection hyperhemispheric lens where a catadiopter containing the frontal optics is designed to have a different focal length without any interference between the frontal FoV and the panoramic FoV when they are imaged on the focal plane.

For our analysis we can treat this peculiar lens as a general panoramic lens, since only the panoramic FoV was used to acquire images and test the method.

The lens has been designed to be used with a 2/3-in. matrix sensor, fixing the dimension of the external donut diameter ($2R_{max}$) at 6 mm. The focal length of the on-axis field (paraxial condition) is 2 mm, whereas it changes for the off-axis field according to the anamorphic function described in Eq (3.9) The relative aperture is F/3.5.
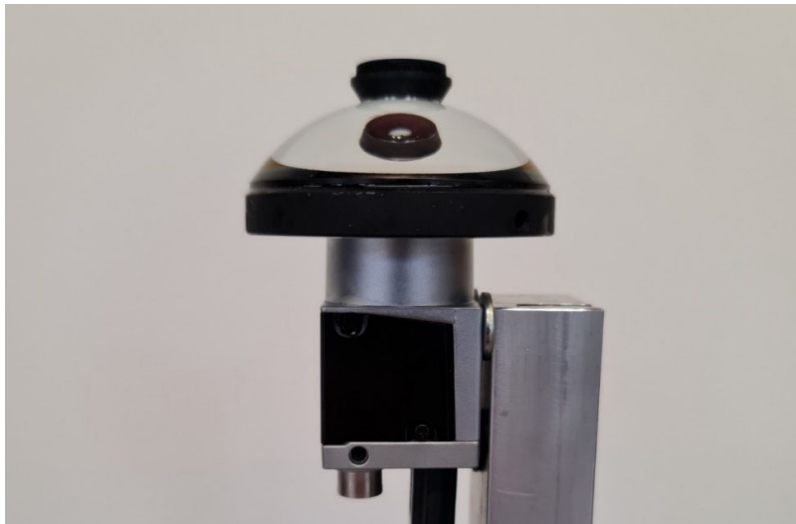

FIGURE 4.1 *THE BIFOCAL HYPER-HEMISPHERIC PANORAMIC LENS USED IN OUR TESTS*
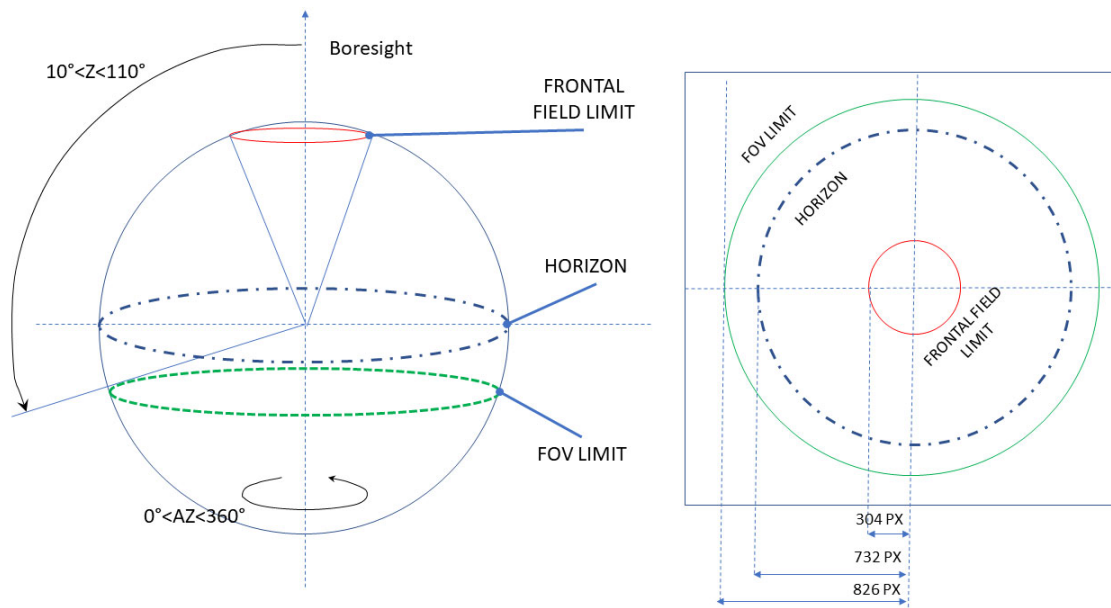
FIGURE 4.2 *FIELD OF VIEW OF THE PANORAMIC FIELD OF THE BPL LENS.*

The BPL (lens) is a very wide-angle lens able to image a Field of View (FoV) of 360° in azimuth angle and up to 220° in elevation (10° < Z < 110°, see Figure 4.2, left panel), the zenith angle Z going from 0° (zenith) up to 135°. Central part of the FoV does not belong to the panoramic field and is not considered in this calibration approach. The entire FoV is imaged by the lens on its focal plane in a way indicate in the right panel of the Figure 4.2.

4.2 Set of images and calibration target

The lens was mounted on an arm support, looking towards ground.

For the lens analysis 45 images were used, displayed in Figure 4.4, with a clearer example in Figure 4.3.

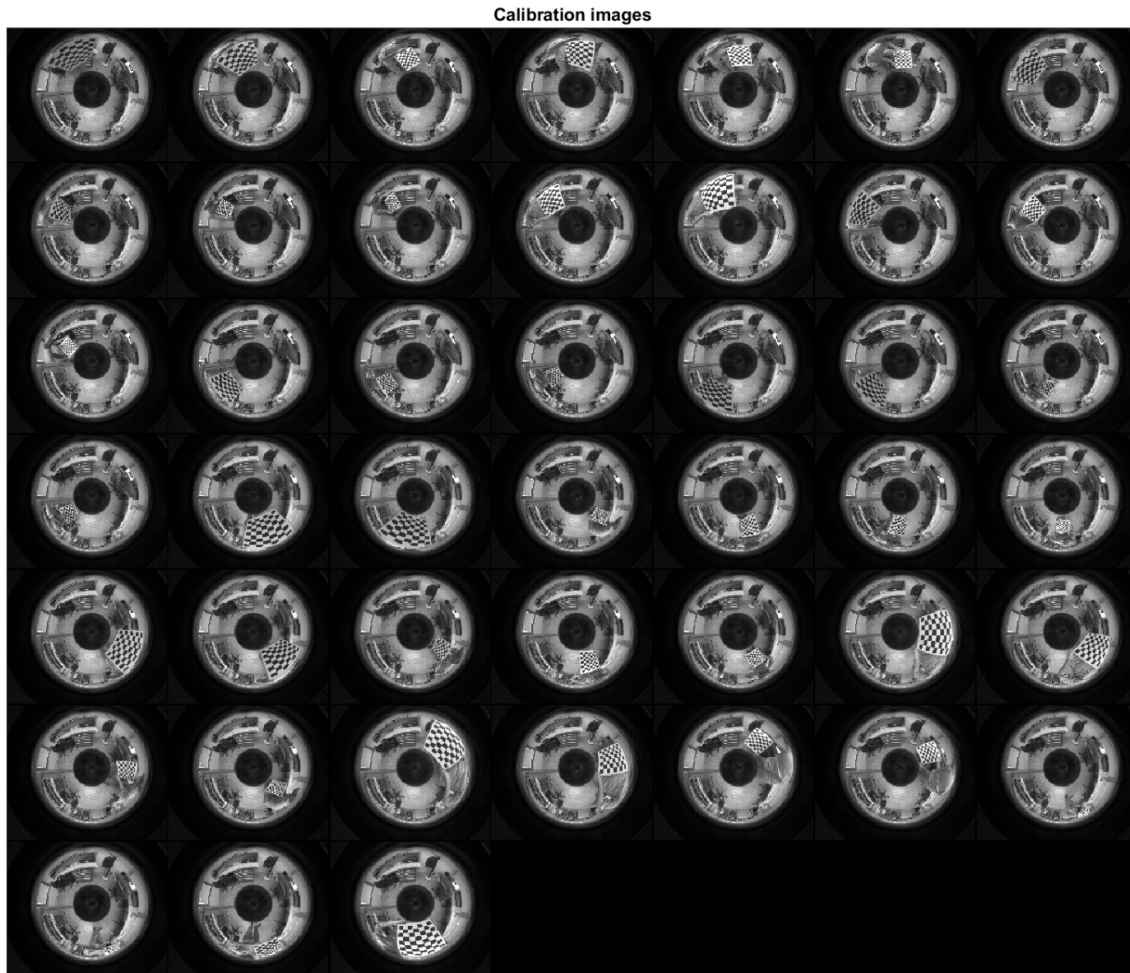**FIGURE 4.3:** *EXAMPLE OF AN IMAGE OF THE SAMPLE*

FIGURE 4.4 *IMAGES SAMPLE*

The images were acquired with a 2/3-in. image sensor and are 2448 x 2048 pixels large. The chessboard, printed and fix on a rigid glass support, is composed by a 7 by 5 grid of black and white squares, with a 42.5 cm side. The images show the chessboard from several positions and orientations, covering almost 360° in azimuthal angle (a small section is obstructed by the arm support) and quite the full panoramic FoV in zenith angle, with a focus between 30° and 90°.

The code was not able to automatically recognize all corners only in four images, for two of which the missing ones were added manually. For the other two all the corners were detected manually.

4.3 Results

In the following subsections the analysis results will be uncovered and discussed.

The calibration defined for each image the position and the attitude of the target. A plot of the result of this estimation is shown in Figure 4.5.
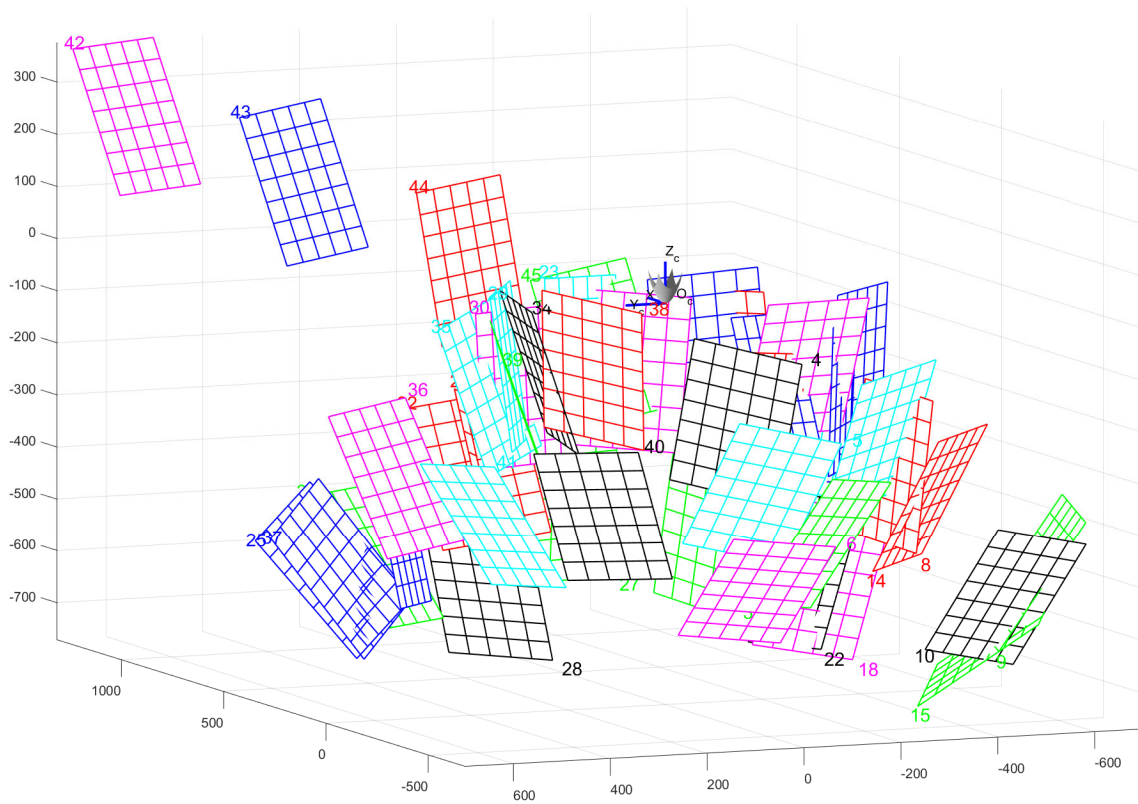
FIGURE 4.5: *A PICTURE OF THE SIMULATOR SHOWING THE CALIBRATION PATTERNS AND THE VIRTUAL OMNIDIRECTIONAL CAMERA AT THE AXIS ORIGIN AFTER THE CALIBRATION, ALL THE PARAMETER CAN BE ACCESSED IN THE TOOL THROUGH THE STRUCTURE "OCAM_MODEL". AXES UNIT IS IN MM.*

4.3.1 Residual analysis

FIGURE 4.6: *RESIDUALS DISTRIBUTION*

Residuals, displayed in Figure 4.6 show a narrow variation of the position of the corners obtained with the calibration.

Horizontal and vertical error in reprojection (corresponding to the residual of the model measured) are limited to a standard deviation of 0.7894 px and 0.7059 px respectively; this means they are contained within 2 px, with just a few corners over this value.

This value should be compared with the error in the detection of the corner performed by Harrys corners (which is limited to 0.5 px).

Figure 4.7 and Figure 4.9 show that the most problematic corners are located at an azimuthal angle just over 0° and at high zenith angle.
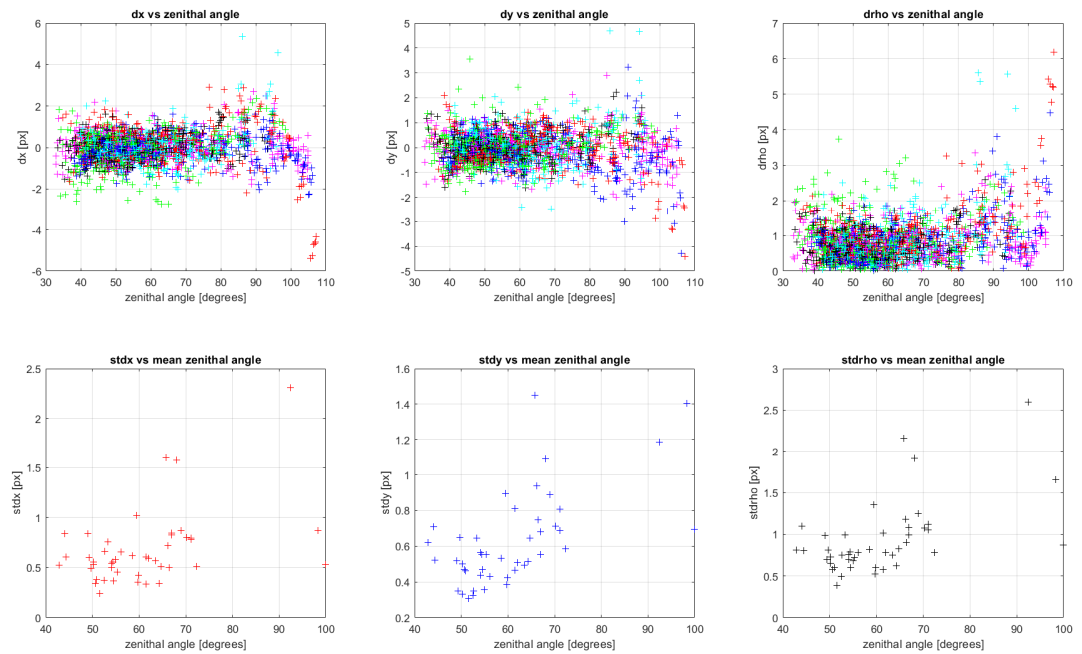

FIGURE 4.7: *ON TOP: DISTRIBUTION OF THE CALIBRATION ERRORS (WITH DIFFERENT COLOR FOR EACH CHESSBOARD) WITH RESPECT TO THE ZENITH ANGLE. FIRST TWO PLOTS SHOW RESPECTIVELY THE HORIZONTAL AND VERTICAL ERROR OF THE REPROJECTION. ON BOTTOM: SAME PLOTS CONSIDERING THE MEAN ERROR OF EACH CHESSBOARD.*

The plot shows a uniform distribution of the error with respect to the zenith angle a part 1 test (red chessboard with zenith angle greater than 100°) where the reprojection error reach more than 4 px. The image considered is shown in Figure 4.8.
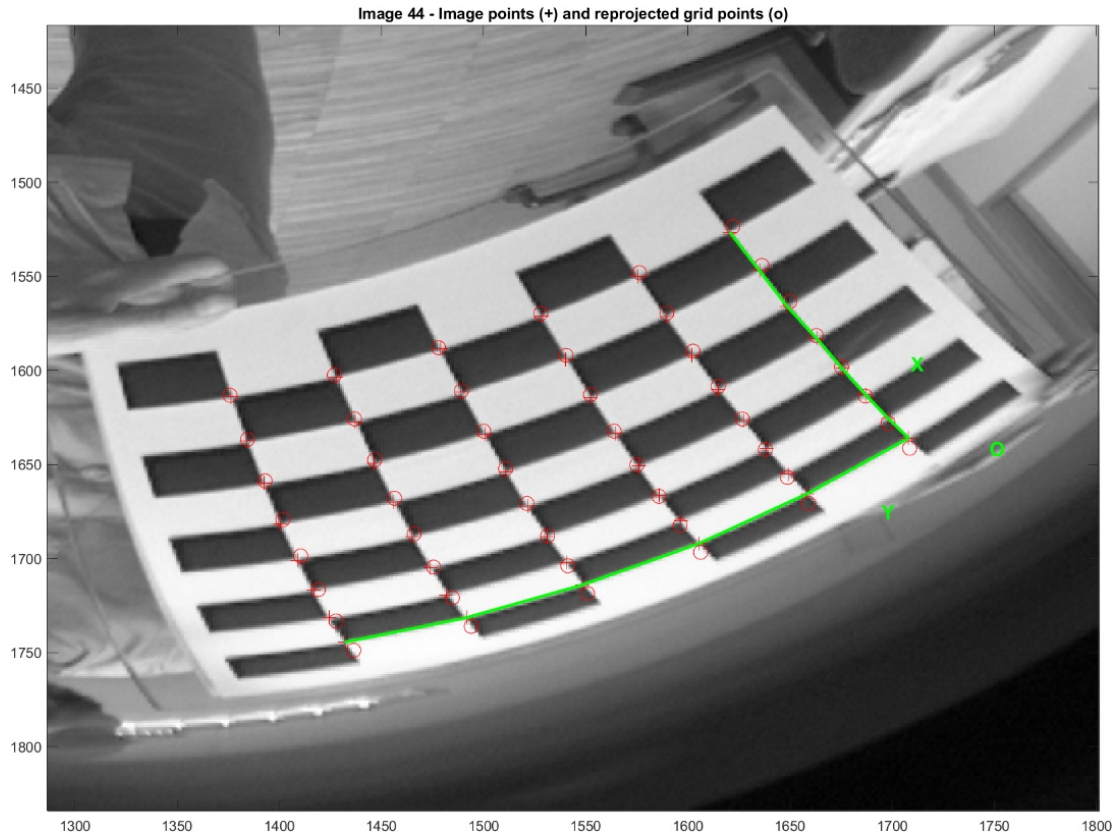
FIGURE 4.8: *CASE OF IMAGE 44 WHERE REPROJECTION ERRORS ARE WORSE THAN EXPECTED*

Considering the anamorphism introduced for high zenith angle it is clear that here the detection error is not compatible with the other acquisitions. For these reason we performed the detection manually in manner to improve the accuracy of the corners definition. Even with this strategy the error remains higher demonstrating that the model is not able to cover the external region of the FoV unless a campaign of acquisition of images covering this region (here covered by 1 image) is performed. The algorithm is fact based on a LM and is optimizing all the acquisitions (most of them have low zenith angle) and in the single case of the BFL the optics parameters are too much different between the sub equator region and the central one.
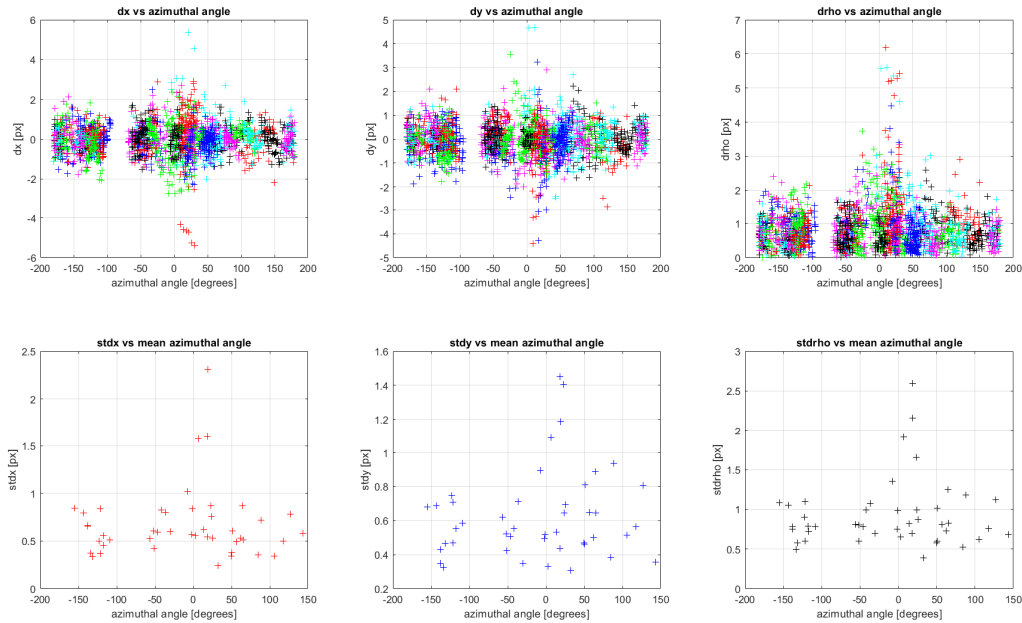
FIGURE 4.9: *ON TOP: DISTRIBUTION OF THE CALIBRATION ERRORS (WITH DIFFERENT COLOR FOR EACH CHESSBOARD) WITH RESPECT TO THE AZIMUTHAL ANGLE. FIRST TWO PLOTS SHOW RESPECTIVELY THE HORIZONTAL AND VERTICAL ERROR OF THE REPROJECTION. ON BOTTOM: SAME PLOTS CONSIDERING THE MEAN ERROR OF EACH CHESSBOARD*

From an azimuth point of view there is no correlation between the residual error and the azimuth demonstrating that the radial model is well representing the camera model.

As exception we have to consider the images 23, 43 and 44 reported in the Figure 4.10 which show a few points having high recalibration errors. Image 44 is a particular case, showing high reprojection errors related both to the zenith angle and the azimuthal angle. This is with high probability due to the fact that the chessboard is located at very high zenith angle. Figures shows how the anamorphism does have not impact on the detection of the corners, but the symmetric polynomial function is not precise enough (for high zenithal angle) to model the geometrical projection; this has an impact on the extrinsic parameters of the chessboard estimation and on their reprojection.

Image 23 - Image points (+) and reprojected grid points (o)
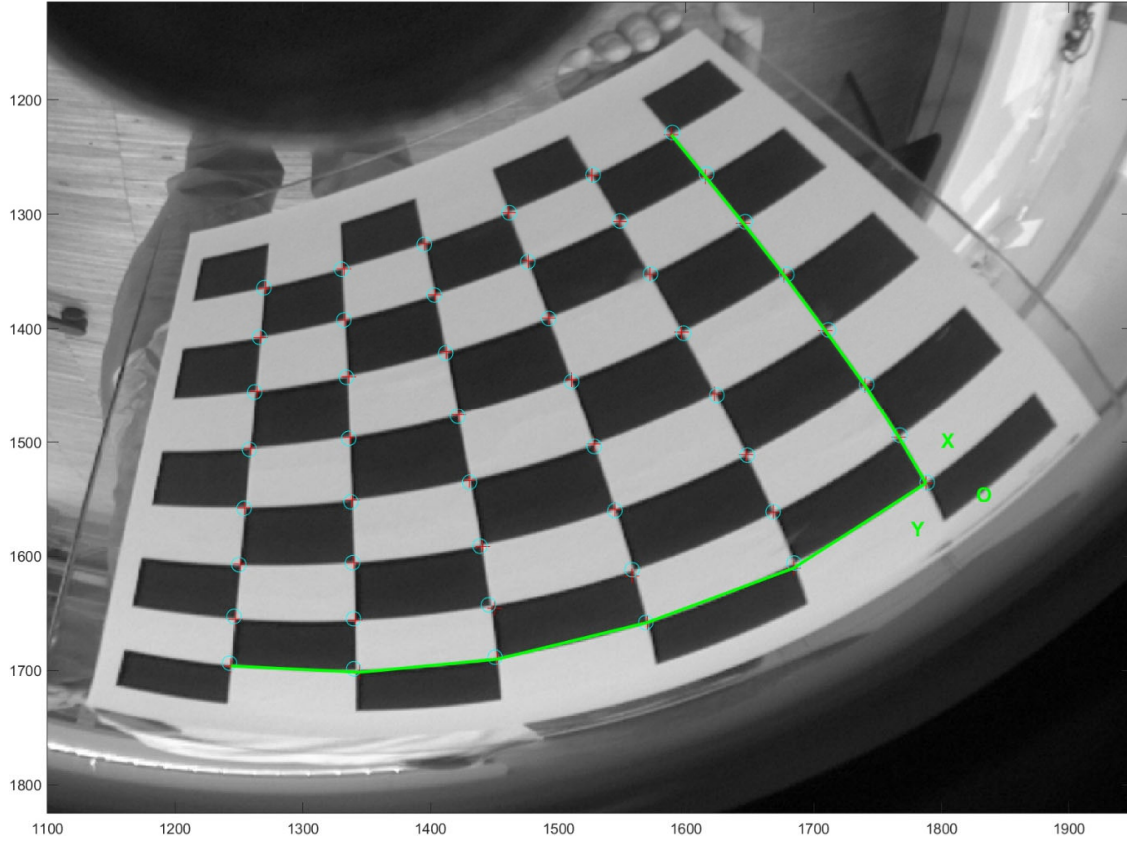
(a)

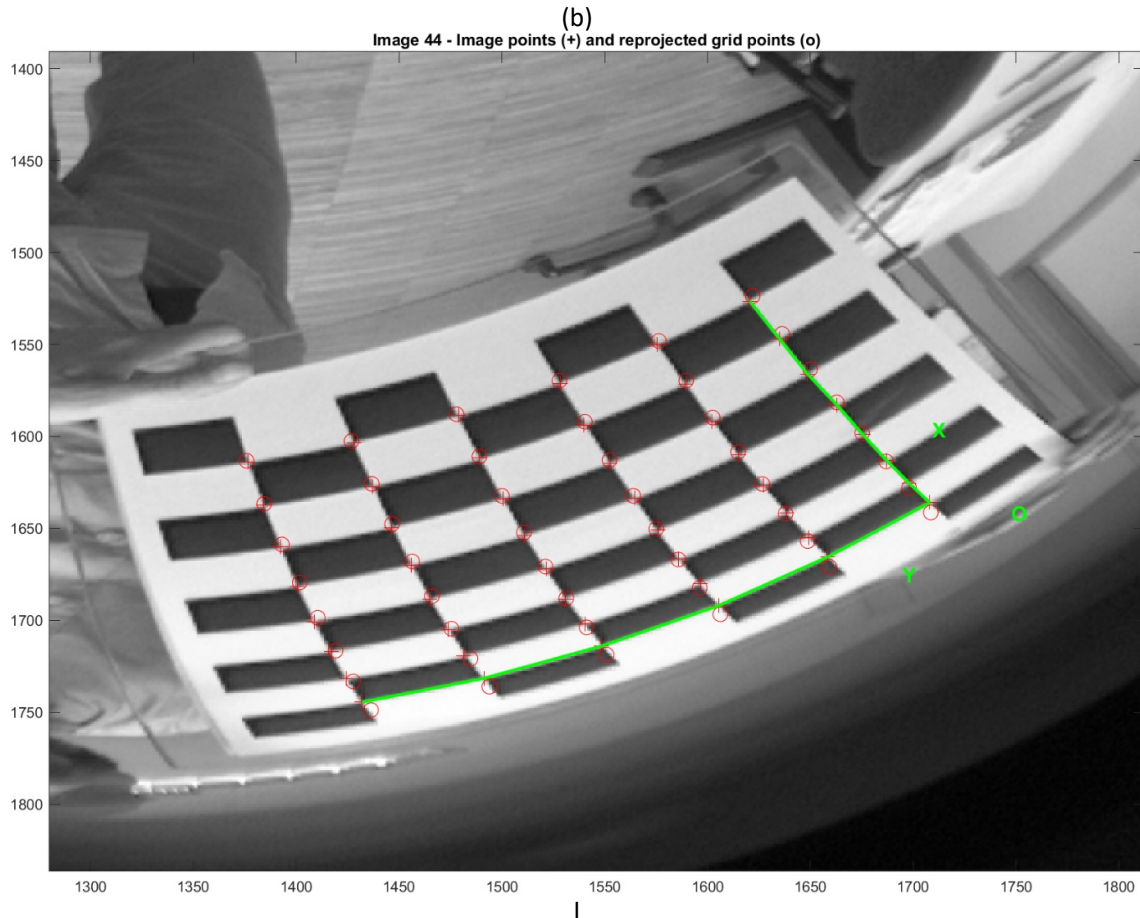**Image 43 - Image points (+) and reprojected grid points (o)**
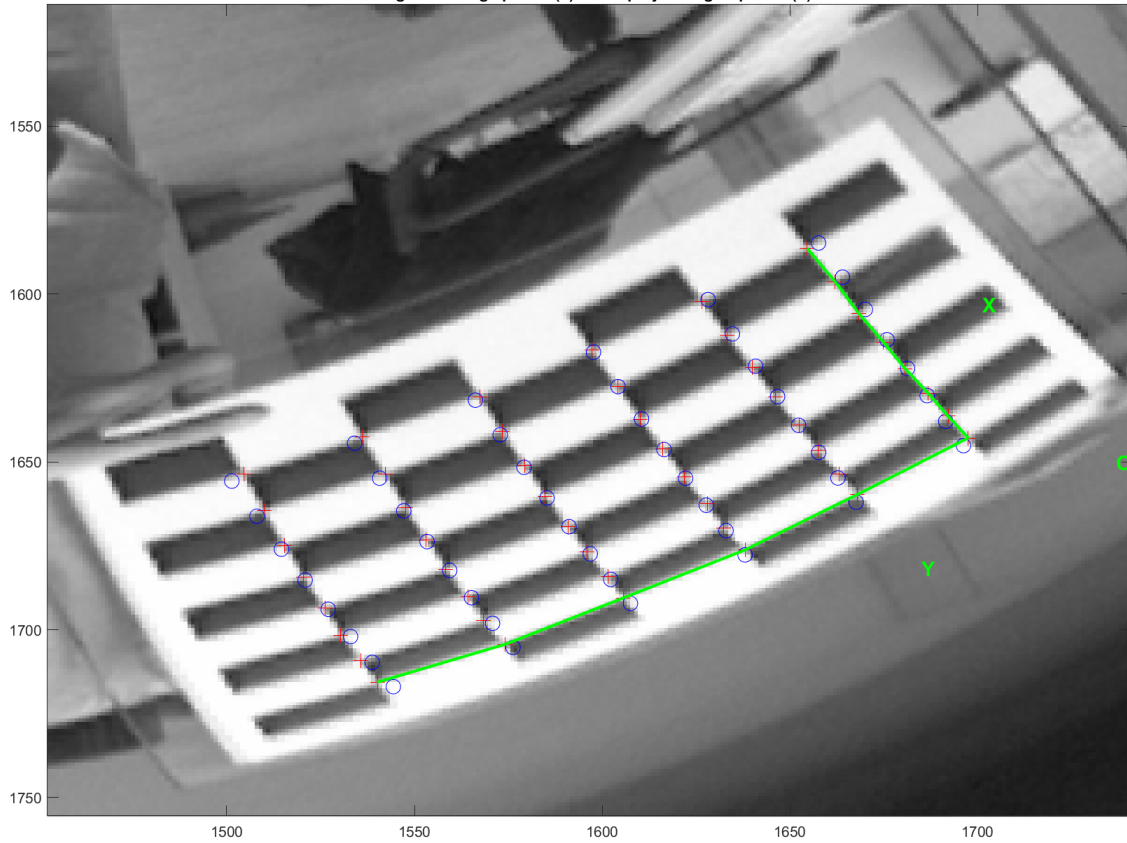
FIGURE 4.10: *THE THREE CASES WHERE THE RECALIBRATION ERRORS SEEM TO BE LINKED TO THE AZIMUTHAL ANGLE, IMAGE 23 IN (A), IMAGE 43 IN (B) AND IMAGE 44 IN (C)*

Despite all these considerations, the errors were generally low enough to consider mostly good the calibration obtained with the code.

4.3.2 IFOV measurement

Starting from the obtained polynomial model it was possible to estimate the IfoV of the system for each distance from the boresight. The IfoV is obtainable, as quoted in section 3.1.2, as the first derivative of Eq. (3.6).

$$\dot{\theta} = \dot{p}(\rho) \tag{4.1}$$

Results are displayed in Figure 4.11. The model application to the whole sensor shows the correct monotony of the IFOV and a 16 mrad/px peak at the edge of the sensor. However, the real image obtained with the lens (due to the real FoV) is confined within 826 px from the image center, locking the IfoV within 4 mrad/px. In particular, there are good results for zenith angles lower than 80°, even though even at higher angles the IfoV is good enough, accordingly to the expectation values of 1-3.5 mrad/px.
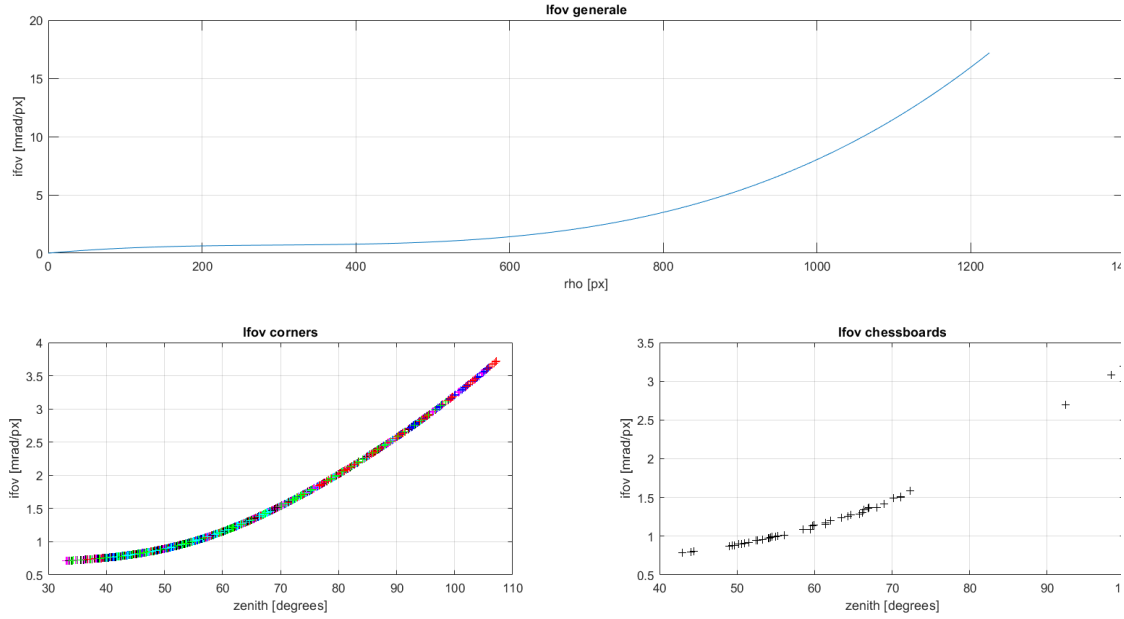
FIGURE 4.11: *ON TOP: GENERAL IFOV CALCULATED OVER THE WHOLE SENSOR; BOTTOM LEFT: IFOV OF THE SINGLE CORNERS; BOTTOM RIGHT: IFOV OF THE MEAN POINT OF EACH CHESSBOARD*

4.3.3   Lens constant

As a final test we tried to obtain the constants k_2, dk_1 of the general lens mapping function, Eq (3.9).

Firstly we searched for the values of the constants with a direct method. Since Eq (3.9) is not analytically solvable an iterative research is necessary. From the starting equation, using two sets of values (Z_A, ρ_A) and (Z_B, ρ_B), the following equation is derived:

$$\frac{\rho_A}{\rho_B} = \frac{dk_1 \sin(k_2 Z_A)}{dk_1 \sin(k_2 Z_B)},$$ (4.2)

where ρ and Z are the position of a corner on the sensor with respect to the lens reference system and its zenith angle, taken in pairs for two corners of the images (here identified by A and B).
The previous equation can be simplified as

$$\rho_A \sin(k_2 Z_B) - \rho_B \sin(k_2 Z_A) = 0.$$ (4.3)

We coupled each corner with all the other corners in the same image and looked by iteration for the correct value of k2. We moved k_2 inside the interval]0.0001,1.3332[by a 0.0001 step and kept the value which minimize the residual from the difference in Eq.   (4.3). The extremes of the interval were chosen in this way since 0 and 4/3 are the minimum and the maximum values which set the argument of the sinus equal to 0 for the minimum and the maximum values among all the possible zenith angles for this lens, respectively. For each corner we took than the average value among all the couples. From each k_2 a value for dk_1 was then retrieved as

$$\boldsymbol{dk_1} = \frac{\rho}{\sin k_2 Z}.$$ (4.4)

Results are shown in

Figure 4.12 and

Figure 4.13. The mean values for $k_2 = 0.738 \pm 0.0425$ and $dk_1 = 2.7254 \pm 0.1186$. These values are then used as base values for a nonlinear least-squares algorithm, callable in MATLAB as "*lsqnonlin*", which returns $k_2 = 0.6950$ and $dk_1 = 2.8576$. The residuals are calculated as the difference res $= \rho - dk_1 \sin(k_2 Z)$.
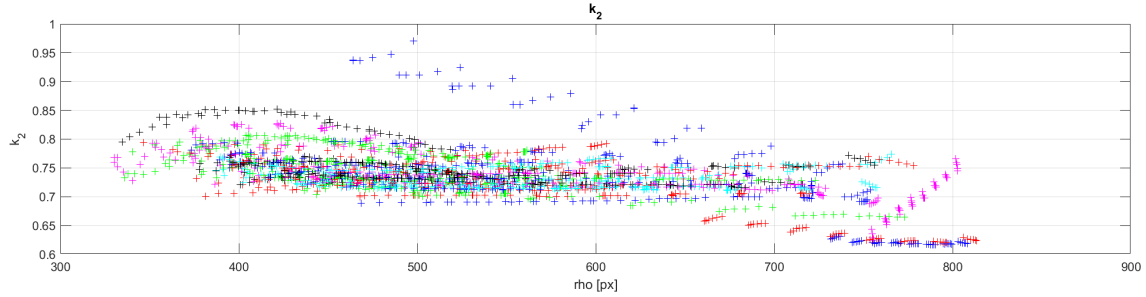
FIGURE 4.12*: VALUES OBTAINED FOR THE CONSTANT* k_2
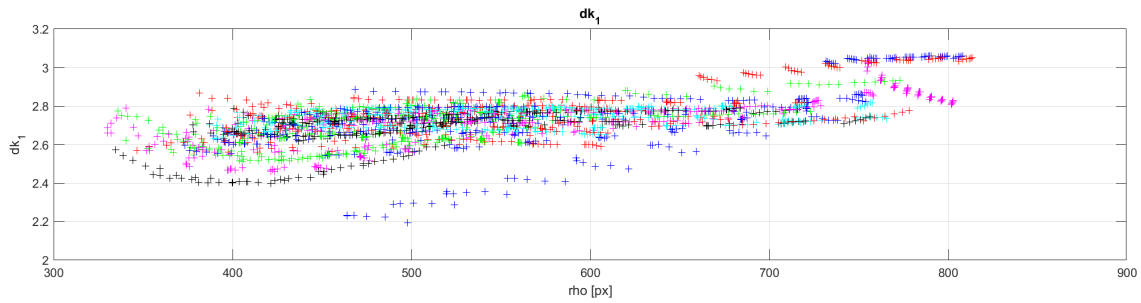
FIGURE 4.13: *VALUES OBTAINED FOR THE CONSTANT* dk_1

We repeated the analysis with a different approach. Using the values of the positions of the corners on the sensor with respect to the lens reference system ρ and their related zenith angle Z we applied the nonlinear least-squares evaluation separately on each single chessboard. The mean values for the constants obtained, averaged over all the chessboards, are $k_2 = 0.7209$ and $dk_1 = 2.7719$. This were subsequently used as base values for a nonlinear least-squares evaluation on all the corners of the chessboards, taken all together. The results of this independent evaluation are exactly the same as before, with $k_2 = 0.6950$ and $dk_1 = 2.8576$. In

Figure 4.14 and Figure 4.15 are displayed the residuals of the methods in relation to the corners and to the distance ρ from the center of the lens projection.
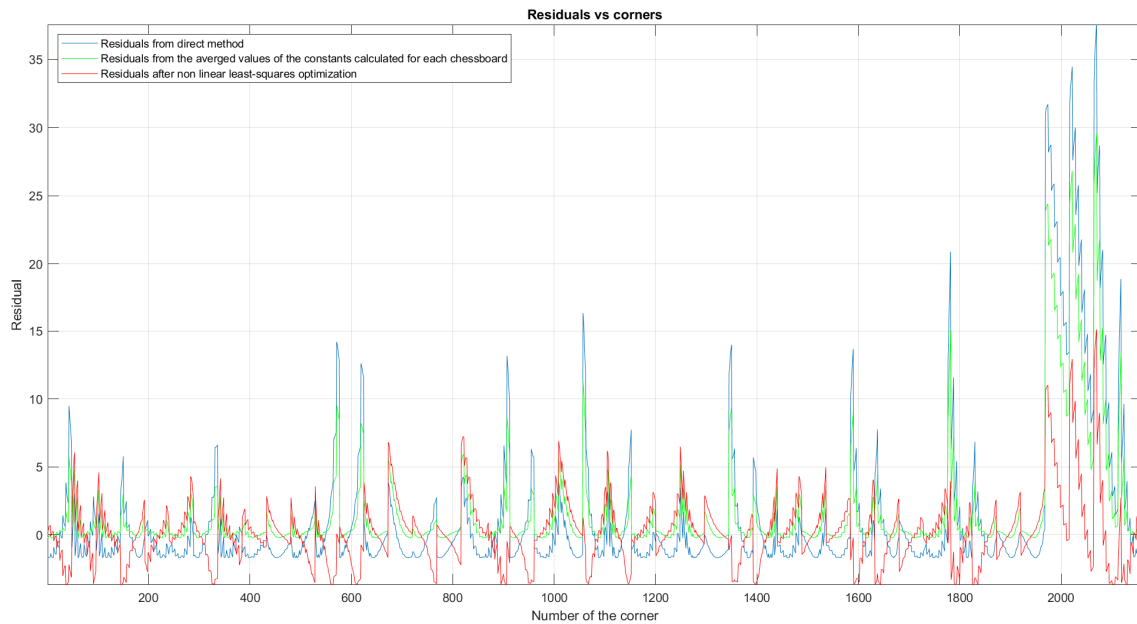
FIGURE 4.14: *RESIDUALS FOR EACH CORNER OF THE SAMPLE. IN BLUE THE RESIDUALS OBTAINED WITH THE FIRST (DIRECT) METHOD, IN GREEN THE RESIDUAL USING THE AVERAGED VALUES OF THE CONSTANTS CALCULATED FOR EACH CHESSBOARD, IN RED THE RESIDUALS AFTER THE NONLINEAR LEAST-SQUARES EVALUATION*

FIGURE 4.15: *RESIDUALS DISTRIBUTION WITH RESPECT TO THE DISTANCE FROM THE CENTER OF THE LENS PROJECTION ON THE SENSOR. IN BLUE THE RESIDUALS OBTAINED WITH THE FIRST (DIRECT) METHOD, IN GREEN THE RESIDUAL USING THE AVERAGED VALUES OF THE CONSTANTS CALCULATED FOR EACH CHESSBOARD, IN RED THE RESIDUALS AFTER THE NONLINEAR LEAST-SQUARES EVALUATION*

It Is possible to see that with this last method we are able to retrieve the same values for the constants even with random, although reasonable, starting values for k_2 and dk_1. The following figures show the same plots of the residuals with starting values $dk_1 = 5$ and $k_2 = 0.3$, resulting in the same dk_1 and k_2 found earlier after the nonlinear least-squares evaluation.

FIGURE 4.16: *RESIDUALS FOR EACH CORNER OF THE SAMPLE, IN BLUE THE RESIDUALS FOR $dk_1 = 5$ AND $k_2 = 0.3$, IN RED THE RESIDUALS AFTER THE NONLINEAR LEAST-SQUARES EVALUATION*
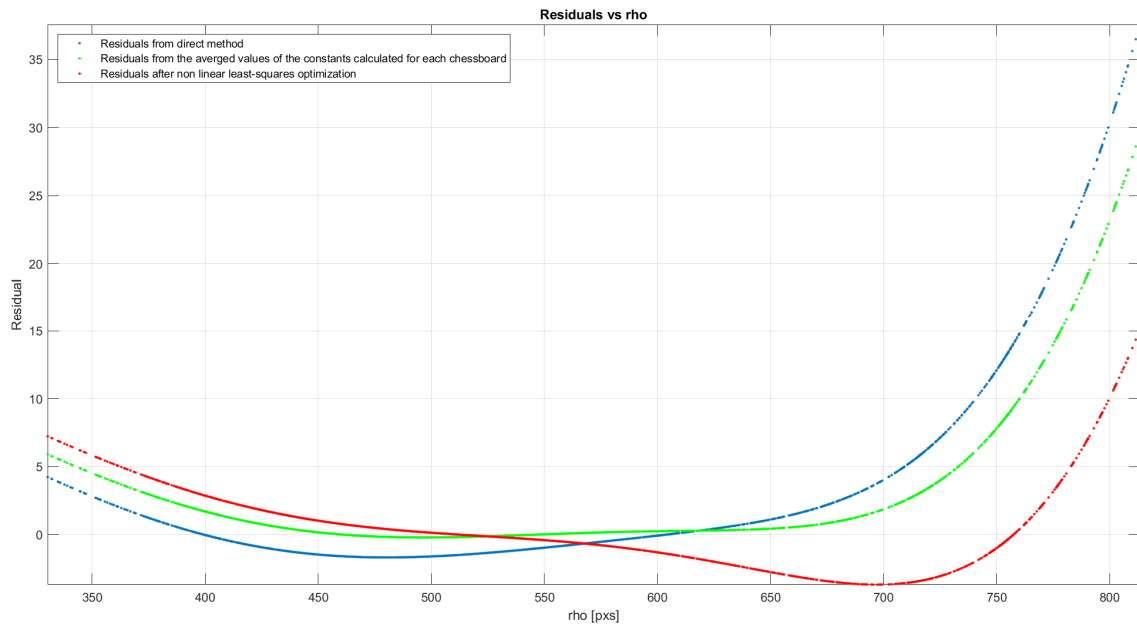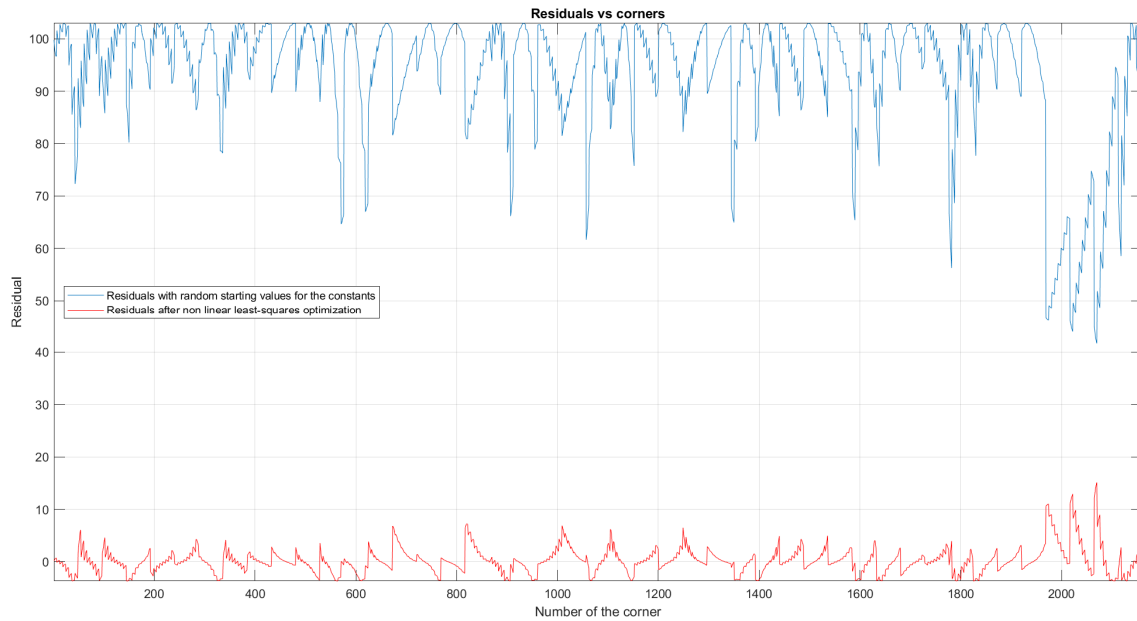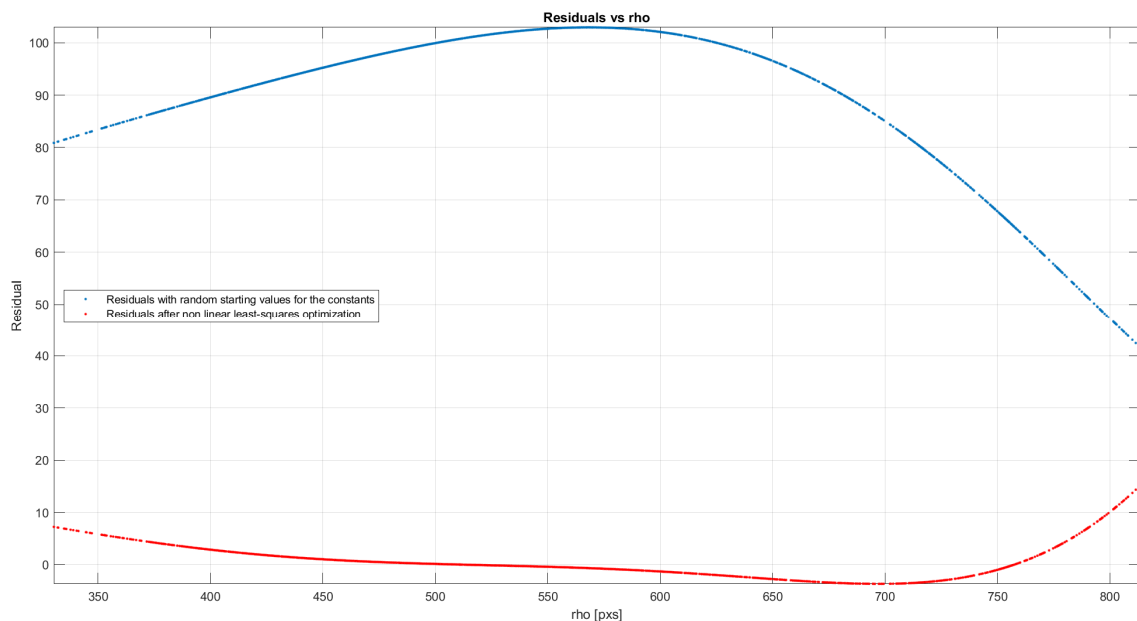

FIGURE 4.17: *RESIDUALS DISTRIBUTION WITH RESPECT TO THE DISTANCE FROM THE CENTER OF THE LENS PROJECTION ON THE SENSOR, IN BLUE THE RESIDUALS FOR $dk_1 = 5$ AND $k_2 = 0.3$, IN RED THE RESIDUALS AFTER THE NONLINEAR LEAST-SQUARES EVALUATION*

5 Tables of data results

In this section are reported the most valuable parameters associated to each image as defined in this following reference table:

ID_IMAGE	#	name of the k-th image
MEAN_POS_i_REFC0	[px]	mean horizontal position in the lens reference system
MEAN_POS_j_REFC0	[px]	mean vertical position in the lens reference system
MEAN_POS_i	[px]	mean horizontal position in the sensor reference system
MEAN_POS_j	[px]	mean vertical position in the sensor reference system
AZ	[°]	mean azimuth angle
ZEN	[°]	mean zenith angle
DIST	[px]	mean corner distance from the center of the lens
ERR_i	[px]	mean horizontal residual
ERR_j	[px]	mean vertical residual
STD_i	[px]	standard deviation of the horizontal residuals
STD_j	[px]	standard deviation of the vertical residuals

ID IMAGE #	MEAN POS_i (REFC0) [px]	MEAN POS_j (REFC0) [px]	MEAN POS_i [px]	MEAN POS_j [px]	AZ [°]	ZEN [°]	DIST [px]	ERR_i [px]	ERR_j [px]	STD_i [px]	STD_j [px]
1	-523.06	-238.48	424.11	1061.19	-155.30	66.96	592.24	0.02	-0.28	0.85	0.68
2	-471.92	-167.13	475.22	1132.53	-137.94	56.08	514.54	-0.08	0.09	0.65	0.43
3	-476.64	-101.27	470.48	1198.38	-138.17	52.65	491.95	0.13	-0.04	0.66	0.35
4	-559.98	16.69	387.09	1316.37	-1.91	63.52	568.34	-0.03	0.27	0.57	0.49
5	-530.13	9.99	416.94	1309.66	13.80	58.51	535.96	-0.11	0.09	0.62	0.53
6	-467.58	42.99	479.47	1342.65	62.17	50.26	473.36	-0.06	0.02	0.53	0.50
7	-310.88	-485.05	636.38	814.57	-122.69	66.41	588.42	0.06	0.07	0.50	0.75
8	-234.99	-449.74	712.25	849.87	-117.27	55.27	511.40	-0.29	0.08	0.46	0.56
9	-264.78	-430.21	682.45	869.40	-121.64	54.54	507.51	-0.04	-0.07	0.37	0.47
10	-338.05	-354.31	609.16	945.32	-133.60	52.51	491.64	-0.17	-0.01	0.37	0.32
11	-368.66	-406.53	578.57	893.11	-132.02	61.44	556.17	-0.17	-0.04	0.34	0.46
12	-484.59	-357.96	462.63	941.70	-143.18	71.13	616.01	-0.06	0.25	0.79	0.69
13	-197.56	-586.13	749.73	713.46	-108.74	72.40	627.30	0.22	-0.06	0.51	0.59
14	-235.12	-441.26	712.11	858.35	-117.95	54.34	504.82	0.13	0.06	0.56	0.55
15	-219.25	-358.86	727.95	940.74	-121.35	44.09	423.41	-0.48	-0.43	0.84	0.71
16	381.86	-397.77	1329.03	901.70	-46.22	62.05	560.24	0.33	-0.08	0.60	0.51
17	339.60	-425.40	1286.78	874.08	-51.39	59.90	547.71	0.04	-0.09	0.43	0.42
18	225.94	-342.01	1173.10	957.49	-56.50	42.91	413.50	0.00	-0.05	0.52	0.62
19	480.11	-359.74	1427.25	939.71	-36.68	70.20	612.75	-0.12	-0.50	0.80	0.71
20	435.07	-387.46	1382.23	912.00	-41.92	66.95	593.19	-0.07	0.38	0.83	0.55
21	399.68	-236.52	1346.78	1062.95	-30.47	49.35	466.30	0.11	-0.10	0.60	0.35
22	261.93	-331.93	1209.08	967.56	-51.76	44.41	426.00	0.05	0.19	0.61	0.52
23	527.98	173.08	1474.91	1472.52	18.41	65.82	578.41	0.35	0.38	1.60	1.45
24	510.28	-66.63	1457.30	1232.81	-7.67	59.48	535.93	0.29	-0.22	1.02	0.89
25	304.33	367.36	1251.20	1666.84	50.25	50.98	479.43	-0.11	0.07	0.38	0.46
26	474.71	154.05	1421.65	1453.50	18.14	54.07	502.79	0.25	-0.13	0.54	0.44
27	460.30	-9.68	1407.31	1289.77	-1.14	49.02	463.22	-0.14	-0.17	0.84	0.52
28	471.11	22.99	1418.10	1322.44	2.84	50.23	473.76	-0.03	0.05	0.56	0.33

29	250.04	529.37	1196.85	1828.87	64.62	68.97	602.17	0.09	0.00	0.87	0.89
30	337.26	420.07	1284.10	1719.55	50.94	61.43	551.89	0.26	0.00	0.60	0.81
31	257.02	387.68	1203.88	1687.17	56.70	49.69	468.76	-0.19	0.06	0.49	0.65
32	451.09	198.71	1398.01	1498.16	23.87	53.35	496.90	0.46	0.08	0.76	0.65
33	406.34	257.65	1353.24	1557.12	32.38	51.54	483.93	0.10	0.04	0.24	0.31
34	14.84	560.23	961.65	1859.78	88.36	66.19	581.23	0.19	-0.03	0.72	0.94
35	235.08	514.45	1181.89	1813.95	65.27	64.74	575.74	-0.13	0.19	0.51	0.65
36	53.41	539.35	1000.22	1838.89	84.46	59.77	545.66	-0.06	0.05	0.36	0.38
37	305.34	361.94	1252.20	1661.43	49.69	50.59	476.31	-0.12	-0.17	0.34	0.47
38	-359.13	473.26	587.75	1772.89	126.96	71.10	614.17	-0.20	-0.33	0.78	0.81
39	-151.96	544.38	794.87	1843.97	105.48	64.30	573.38	0.29	0.04	0.34	0.52
40	-402.36	303.67	544.59	1603.31	143.02	55.00	509.62	-0.03	-0.10	0.58	0.36
41	-228.50	442.47	718.38	1742.08	117.39	54.10	502.98	0.12	0.13	0.50	0.56
42	703.66	333.32	1650.51	1632.72	25.35	99.93	779.74	-0.19	-0.25	0.53	0.69
43	707.84	302.70	1654.70	1602.10	23.15	98.32	772.06	-0.56	-0.44	0.87	1.41
44	695.85	240.21	1642.73	1539.61	19.03	92.43	742.42	0.12	-0.51	2.31	1.19
45	566.09	68.26	1513.06	1367.69	6.63	68.07	592.94	-0.58	0.49	1.57	1.09